ABSTRACT

Title of Document: ASSEMBLY AND COMBUSTION PROPERTIES OF ENERGETIC MESOPARTICLES

Boran Wei, Master of Science, 2015

Directed by: Prof. Michael R. Zachariah
Department of Chemical and Biomolecular Engineering

Energetic materials are materials which can release large amounts of energy in a short time interval. When the size of energetic materials is reduced from micro into nanoscale, the reactivity of energetic materials increases dramatically due to increase in intimate contact and faster mass and heat transfer. Finding an efficient way to synthesize energetic nanocomposites has become an import research topic. Here I demonstrate the use of electrospray methods to generate mesostructured microparticles containing nanomaterials and a gas generator. The system was designed for characterization of the size distribution as well as combustion properties. In this thesis, size distribution of the Al/NC mesoparticles is tuned from 0.7-2.0 μm, and the ignition delay is shown significantly decrease (15 ms to 3 ms) compared to nano-size Al. The burn time is also decreased significantly (4036 μs to 366 μs) by using electrospray assembly. This demonstrated that assembly of nanocomponents can significantly impact combustion performance.

ASSEMBLY AND COMBUSTION PROPERTIES OF ENERGETIC MESOPARTICLES

by

Boran Wei

Thesis submitted to the Faculty of the Graduate School of the
University of Maryland, College Park, in partial fulfillment
of the requirements for the degree of
Master of Science
2015

Advisory Committee:

Prof. Michael R. Zachariah, Chair
Prof. Sheryl H. Ehrman
Prof. Chunsheng Wang

Dedication

This thesis dedicated to my parents,

Li Yu and Dongping Wei,

谨以此文献给我的母亲 于丽，父亲 尉东平

for their unconditional love, invaluable efforts.

感谢你们毫无保留的爱和无私的奉献

This work wouldn’t be possible without you.

是你们成就了今天的我

Acknowledgement

I would like to thank Dr. Michael R. Zachariah, who gave me the opportunity to join his group and guided me through my whole graduate study. It is my honor for being his student and have the chance to learn his experience and insight in research as well as his deep understanding in chemical engineering.

I would also like to thank our lab group members. They not only offer me a lot of help during the research, but also help me a lot in my personal life. It is my greatest pleasure to work with them.

I would also like to thank all my friends especially my roommates Zan Wang and Xihang Xu, who never hesitated to help me no matter what difficulties I have. It is a great journey for study abroad in United States and I'm grateful I have them with me.

At last but not least, I would like to thank my parents. They spend a lot on me to ensure that I can have good living condition and education. If anyone believe that I can make it, it will be them.

Boran Wei

尉 博 然

Table of Contents

List of Tables

List of Figures

Chapter 1: Introduction and Overview

Energetic materials, especially in micro and nano size, are of interest due to their advantages such like high energy density, fast and controllable release rate, etc. In this thesis, I will focus on the aluminum particles and aluminum-based nanothermites, which have very wide applications like additives for propellant, dynamites, igniter, etc.

Though lots of research have been done by our group and other researchers, there are still some blanks need to be fill in this area. For example, which technique should we choose to produce energetic mesoparticles? What is the relationship between morphology and combustion property for energetic mesoparticles? etc.

In order to answer these questions, lots of research have been conduct by our group, especially on using electrospray to synthesize desired energetic mesoparticles. Figure 1.1 shows the typical setup for electrospray method.[1] The reason for us to focus on electrospray approach is the advantages electrospray have over other methods. For example, ability to control particle size, very narrow particle size distribution, easy to setup and operate, etc. However, by using electrospray, we are unable to obtain the size distribution *in-situ*. This thesis introduces a new approach of electrospray assembly method which can not only assemble energetic materials, but also able to conduct measurement like size distribution, combustion speed, etc. *in-situ*. With the help of the new setup, we are able to study what is the impact of changing different variables like nitrocellulose (NC) wt%, solvent, voltage, etc. on the particle combustion.

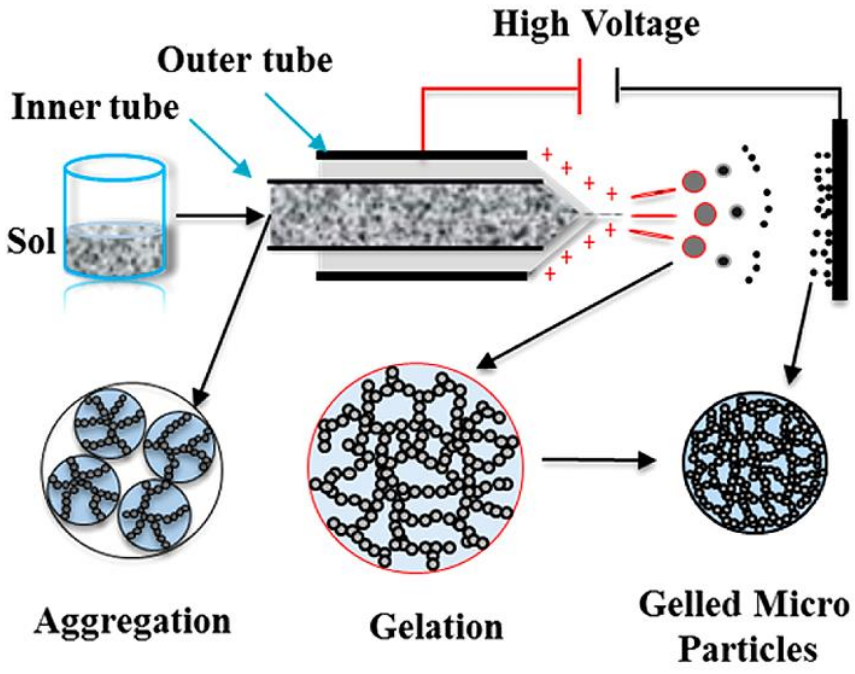

Figure 1.1 Typical setup for electrospray method.[1] Fluid pumped out from the nozzle by syringe pump and form droplet at the tip of the nozzle. A voltage is implied between the nozzle and substrate to create the electric field.

In this thesis, background information on electrospray, aluminum and aluminum-based nanothermite and other key concepts will be introduced in chapter 2. In chapter 3, a detailed description of electrospray assembly will be presented. Theory and models regarding about electrospray will be explained as well as the experimental work. Using electrospray, we are able to assemble energetic mesoparticles which have controllable and uniform size and morphology. Chapter 4 will focus on the new setup of electrospray particle generator. This particle generator enable us on various optional for measurement, test and further experiment. Also, I will describe and discuss the combustion property of

the energetic mesoparticles. With the help of the new particle generator and high speed burner, we can study the combustion process more thoroughly. The particle burning speed and flame temperature will be study in order to get their relationship with the particle size and other variables (e.g., NC content, solvent, etc.) .Finally, summary and future direction will be discussed in chapter 5.

Chapter 2: Background

In this chapter, I will discuss some basic concepts and theories of electrospray approach and energetic mesoparticles. Then, several characterization techniques which we used in this study will be introduced

.

2.1. Energetic Mesoparticles

Energetic materials are a class of material which have the ability to store large amounts of energy.[2] Applications for energetic materials can be classified based on the time interval of combustion. Propellants and pyrotechnics release their energy through a slow process while explosives release their energy in a very short period.[3, 4] Traditional Energetic material like TNT, HMX, CL-20, etc. are based on mono molecular compounds, which limited their maximum heat due to their reaction enthalpy.[5, 6] Mono molecular energetic materials undergo a rapid exothermic reaction to release energy. The whole reaction process are controlled by the reaction kinetics of molecular decomposition which also indicate that the energy density are relatively low. [7] Higher energy density can be obtained by using metal fuels like Al, Mg, B, etc. Fig 2.1 shows the comparison of mass and volume energy density of different energetic materials.[11] But a major disadvantage of metal fuels is their low reaction rate due to heterogeneous reaction kinetics. Research has shown micron-sized metal particles have a longer ignition delay and slower combustion process compare to mono molecular materials.[8-10] When particle

size shrinks to nano dimensions, the main limitation become gas phase oxygen transport into the inner core through the particle oxide layer.

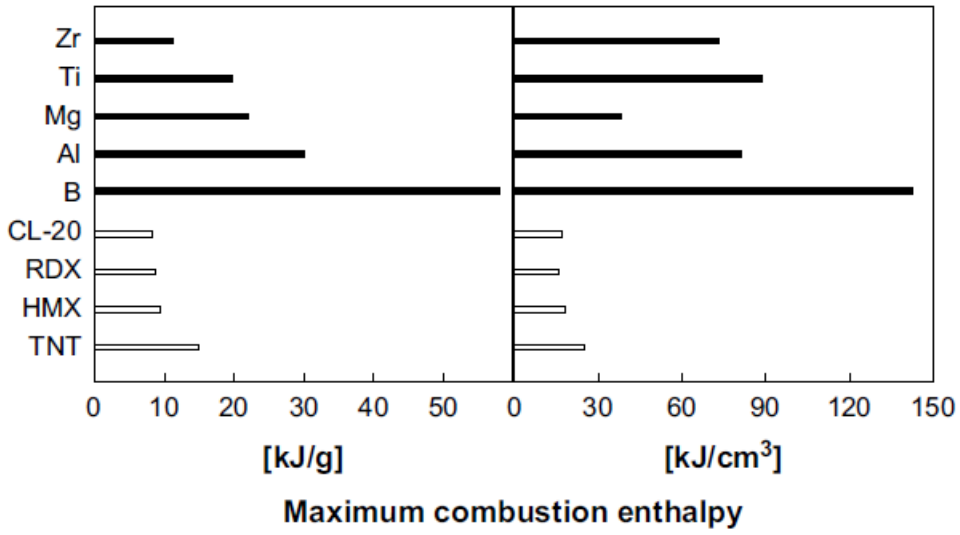

Figure 2.1 Mass and volume energy density of conventional and metal energetic materials[11]

In order to increase the reaction rate, researchers have developed several approaches, which can be categorized in two groups:

1. Mix metal fuel particle with oxidizer (CuO, Fe_2O_3, WO_3, etc.), which is the thermite reaction. With the help of oxidizer, fuel particles undergo a redox reaction which can release large amount of heat.

2. Mix metal fuel particle with binder polymer. (Nitrocellulose) The binder polymer can act as gas generator which release gas and shatter the mesoparticles into small pieces. Then individual small particles can burn faster and more efficiently.

The main idea of these two method are using oxidizer or polymer to form a vapor phase oxidizer surrounding, thus allow faster mass transport of oxygen toward fuel particles. But most conventional micron-sized fuel particle have very poor combustion properties because the agglomeration of aluminum particles before the ignition.[12] The large agglomerates inhibit burning and thus result in longer ignition delay and insufficient combustion.

As the modern manufacturing technology advanced, nano-sized aluminum particles can be manufactured.[13-15] Using nano-sized aluminum particles, I am able to build fuel-oxidizer system that bears higher burning efficiency and quicker response to ignition. This system is metastable, homogenous and its reaction kinetics are not limited to heterogeneous transport process.

This kind of system usually called metastable intermolecular composite (MIC), also known as nano-thermite in energetic material area. The size of the MIC usually around several microns, which can also be addressed as mesoparticles. The scheme of nanothermite is shown in fig 2.2. *Dreizin,* and coworkers showed that in such systems, metastable metal-gas solutions form inside the combusting metal particles.[16] *Zachariah,* and co-workers also studied the oxygen release in this system, and conclude that the oxygen release play an important role in ignition but not required for all oxidizer.

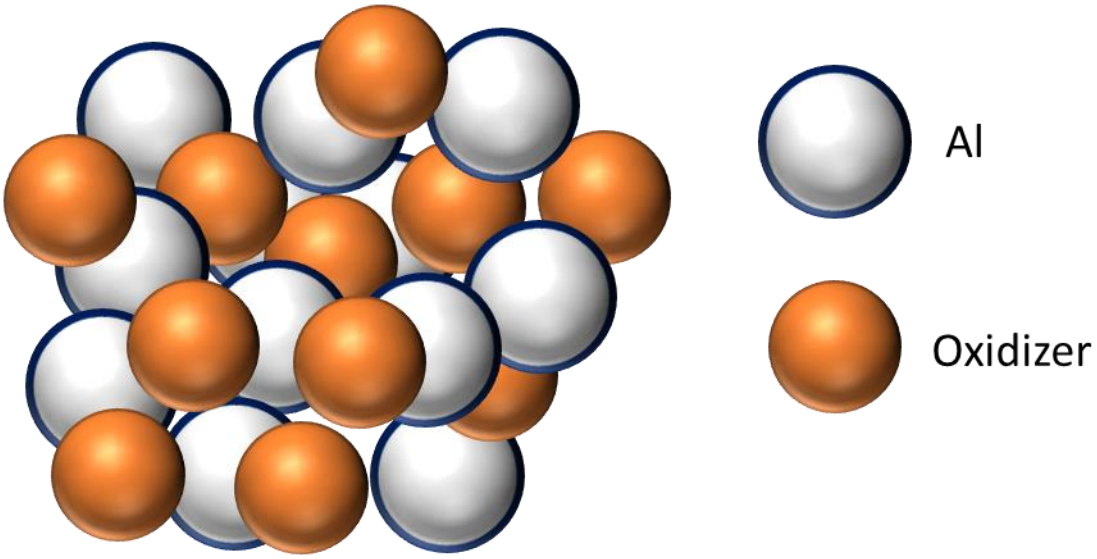

Figure 2.2 Schematic of nano thermite mesoparticles.

Our group's previous research have shown that incorporate nano-sized fuel (most based on Al) and oxidizer to form nanothermite is an efficient way to improve their combustion properties.[17-20, 46-48] But more detailed research on effect of the size and morphology on the combustion still need to be done.

2.2. Electrospray

Electrospray, also known as electrohydrodynamic spray, is a method of liquid atomization assisted with an electric field. In electrospray process, liquid precursor are pumped out of the capillary nozzle and enter the electric field. Induced by the electric field, the liquid undergoing a process of charge accumulation and thus form a conical shape of meniscus at the tip of the nozzle. At the apex of the cone, a filament jet is generated and then break into fine droplets due to Rayleigh instability of the charged liquid.[21] During the whole process, the solvent also undergoing an evaporation process

which will concentrate the precursor and charge in the droplet, thus lead to further chain entanglements and Coulomb fission.[22, 23]

As illustrated in fig 2.3, the bulk forces of the cone-jet and stresses on the liquid surface can be described as following[24], the force is denoted as the volume density.

Table 2.1 Nomenclature of the electrospray model

Nomenclature			
d	droplet diameter	γ_l	liquid bulk conductivity
D	electric flux density	ε_0	permittivity of the free space
E	electric field	ρ_l	mass density of the liquid
F_e	electrodynamic force	ρ_q	volume charge density
F_g	gravitational force	η_l	liquid viscosity
F_ρ	inertial force	σ_l	surface tension of liquid
F_η	drag force	$\Pi_{\Delta p}$	stress tensor due to hydrostatic pressure difference
G	gravity acceleration		
L	volume density	Π_η	stress tensor due to liquid viscosity
P	pressure	Λ_l	tensor of electromagnetic and polarization stress
Q	surface charge density		
v_l	liquid jet velocity	Ξ_i	surface tension tensor
Q	liuqid volume flow rate		

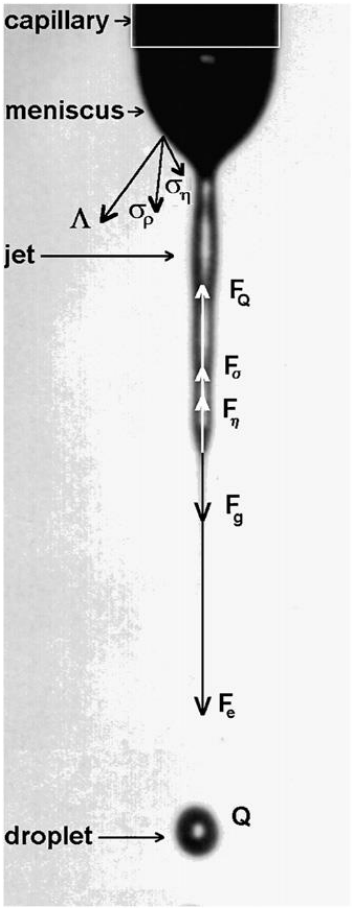

Figure 2.3 Force balance in the electrospray cone-jet.[24]

Electrohydrodynamic force (F_e)

The electrohydrodynamic force is proportional to the strength of electric field, which is the main force acting on the liquid jet.

$$\overrightarrow{L_e} = \rho_q \vec{E} + \frac{1}{2}[\vec{D}\nabla^T \vec{E} - \vec{E}\nabla^T \vec{D}] \quad (1)$$

Gravitational force (F_g):

$$\overrightarrow{L_g} = \rho_l \vec{g} \quad (2)$$

Inertial force (F_ρ):

$$\overrightarrow{L_\rho} = \rho_1 \frac{d\vec{v_l}}{dt} \tag{3}$$

Drag force (F_η):

The drag force in this case can be treated as the Stokes drag. However, due to the complication of the droplet motion, we cannot write drag force in a general form. Several researches have shown that the drag force is proportional to surrounding gas viscosity and jet velocity.[25, 26]

Electrohydrodynamic stress tensor (Λ_l):

Electrohydrodynamic stress are resulting from the combine effect of surface charge and electric field.

$$\vec{\vec{\Lambda}}_l = \vec{q} \otimes \vec{E} + \vec{\vec{l}} * \frac{1}{2}[\vec{D}(\overrightarrow{E_l} - \overrightarrow{E_g}) - \vec{E}(\overrightarrow{D_l} - \overrightarrow{D_g})] \tag{4}$$

Pressure stress tensor (Π_p):

Pressure stress are resulting from the pressure difference between the outside and inside of the jet.

$$\vec{\vec{\Pi}}_p = \vec{\vec{l}}(p_l - p_g)$$

(5)

Viscosity stress tensor (Π_η):

The viscosity stress tensor are pointed in the direction that orthogonal to the liquid surface.

$$\vec{\vec{\Pi}}_\eta = \vec{\vec{\eta}}\nabla\vec{v_l} \tag{6}$$

Inertia stress tensor (Π_ρ):

Inertia stress are resulting from the inertia of liquid and is proportional to the dyadic product of liquid velocity at the local liquid surface.

$$\vec{\vec{\Pi}}_\rho = \rho_l\vec{v_l}\otimes\vec{v_l} \tag{7}$$

From all these forces and stresses, we can derive the force balance as following:

$$\frac{\partial\rho\vec{v_l}}{\partial t} = \rho_l\vec{g} + \vec{L_l} - \vec{\phi_{St}} - \nabla(\vec{\vec{\Pi}}_p + \vec{\vec{\Pi}}_\eta + \vec{\vec{\Pi}}_\rho) \tag{8}$$

$$\nabla\times\vec{\vec{\Xi}} = \vec{\vec{\Pi}}_p + \vec{\vec{\Pi}}_\eta + \vec{\vec{\Pi}}_\rho + \vec{\vec{\Lambda}}_l \tag{9}$$

According to these equations we introduced above, we know that as the charge accumulated on the surface, the surface will become unstable and then form a Taylor-cone.[27, 28] Besides G.I. Taylor, the discoverer of this phenomenon, other researchers also

found that other spray modes may be obtained as the strength of the electric field increased.[29-33] The most common modes are shown in fig 2.4 below.

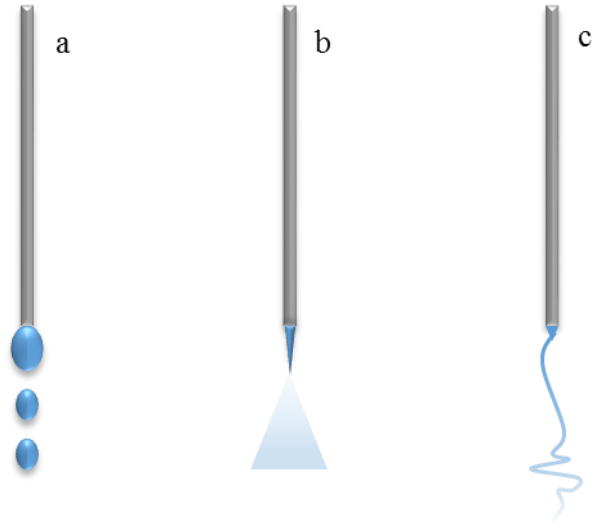

Figure 2.4 Different modes of electrospray. (a) Dripping mode. (b) Cone-jet mode. (c) Spindle mode

Transition between these modes has been explored by a number of researchers [24, 29, 32, 33] *Jaworek, A* have shown that the critical point of transition can be quantitatively analyzed by experiment.[32] (fig 2.5) *Wihelm, O*[34] develop a theoretical model based on mass and momentum transfer to study the evaporation and deposition of electro sprayed droplets. This model shows strong agreement with the experimental data, which conclude that the droplet size have little influence the droplet transfer process. The key parameter to control the droplet size is solvent evaporation, electric field, etc. De La Mora, J. F.[35] investigated the relationship between droplet size and different operating parameters. Swarbrick, J. C[36] studied the electrospray deposition in vacuum and showed that electrospray in vacuum has similar mechanism as in air, with slight size differences in

droplet size. This may indicate that corona charge and surrounding viscosity may not affect the droplet size much.

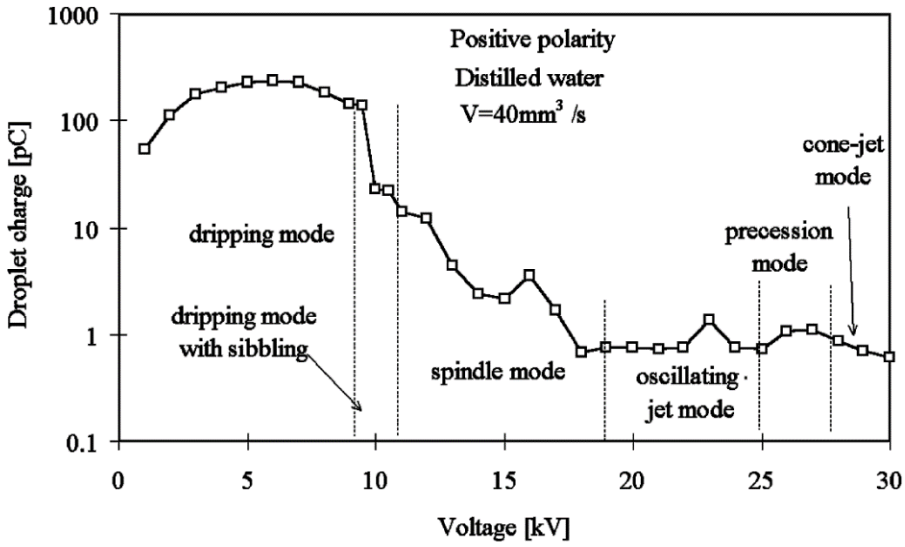

Figure 2.5 Voltage influence on electrospray modes transition[32]

As an assembly method, electrospray offers advantage on many aspects. For example, particles made with electrospray have smaller and more uniformed size than other conventional atomizers; charged droplets are self-dispersed in the space which will not require carrier gas; easy to setup and operate; etc. Because of these merits, a lot of researchers use electrospray to generate micro or nano materials. Jaworek, A and other researchers have been reviewed the application of electrospray on nanotechnology.[24, 27, 37] *Xu, Y, et.al* have use electrospray to do protein encapsulation by chitosan and PLA for tissue engineering.[38, 39] Other biomedical application like drug delivery, gene delivery, wound engagement have also been investigated by other researchers.[22, 40-44] *Shioya, M*, et.al have made PVDF nanofiber by electrospray, which shows controllable size and

morphology.[45] Our group have studied electrospray methods to assembly nano energetic materials which has shown significant improved combustion properties.[46-48]

2.3. Characterization Method

In this thesis, several characterization method will be used to determine the morphology and properties of the energetic mesoparticles. The characterization method we use is listed in the table 2.2 below.

Table 2.2 Morphology and combustion properties characterization method

Morphology	**Combustion Properties**
Scanning Electron Microscope (SEM)	Pressure Cell
Transmission Electron Microscope (TEM)	T-Jump Wire Ignition
Aerodynamic Particle Sizer (APS)	High Speed Particle Tracking Velocimetry

Aerodynamic Particle Sizer (APS) ®

The aerodynamic particle sizer (APS) is a particle size spectrometer to determine particle size distribution from 0.37-20 μm range.[49] The system is shown in fig 2.6.

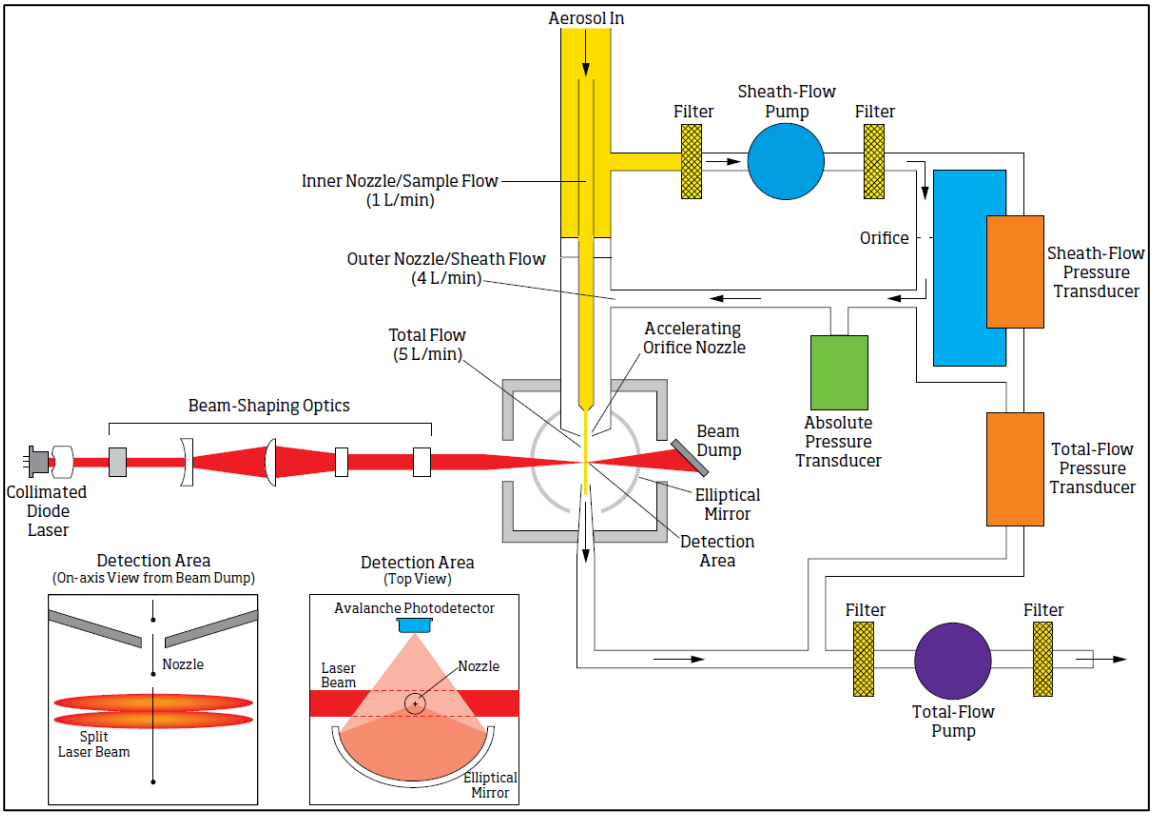

Figure 2.6 Operation scheme of APS.

The APS is designed on dual beam light scattering, where the aerosol first comes into the chamber and be accelerated by carrier gas, while larger particles will accelerate less compare to smaller ones due to increased drag. Particles then pass to detection area, and the two laser beam scattering occurs and detected by the avalanche photo detector. The two beam scattering results in each particle generates a two-crest signal. The time interval of the two signals is recorded and used to calculate the size of particle. This instrument allow one to get the aerodynamic particle size distribution and particle count which when used with the Aerosol Instrument Manager® software can yield a size distribution, which can be fit to log-normal distribution.

Pressure Cell

The combustion performance of the nanothermite is evaluated by a pressure cell measurement. As illustrated in fig 2.7, the pressure cell is made of stainless steel and with a volume of ~13 cm^3. Two sensors, mounted in the sides of the combustion chamber obtain the temporal optical and pressure. In typical operation, 25.0 mg of samples are weighted and placed in the bottom of the combustion chamber. Then samples are ignited by a fast heating nichrome coil. The pressure and optical change are recorded and displayed at the computer for further analysis. Pressurization rate and FWHM burn time can be calculated by this method. More detailed description can be found at our group's previous work.[46]

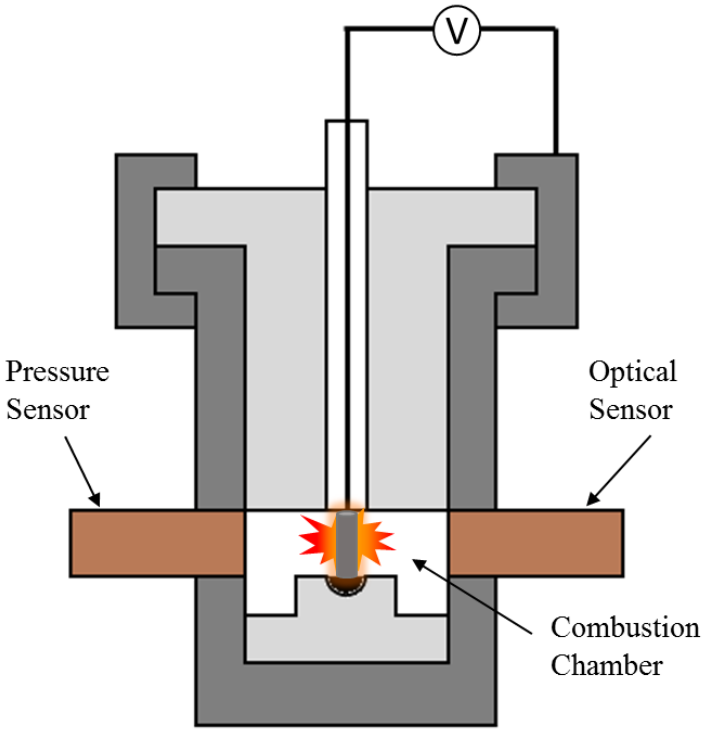

Figure 2.7 Schematic of pressure cell

T-Jump Wire Ignition

In T-Jump wire ignition measurement, a platinum filament of 1 cm long, 76 μm diameter is coated with particle samples. Particle samples are pre-diluted in hexane and ultrasonic for 15 min to achieve homogeneous dispersion. The coated length in that filament is around 4 mm to obtain better observation. Then the filament are connected to a power supply in order to heat it. Once the measurement begin, the power supply is able to heat the wire to 1600 K in 3ms which gives a heating rate of 4×10^5 K/s. Then the combustion process is recorded by a Vision Research Phantom® High-speed Camera, with frame rate of 67,000 fps and resolution of 256×256. The ignition temperature is calculated based on the temporal current and voltage.

Chapter 3: Electrospray Approach for Energetic Mesoparticle Assembly

With all the advantages that nano-sized energetic materials have, many scientists have successfully assembled them by various method like sol-gel[50], DNA-directed assembly[51], arrested reactive milling (ARM)[52], etc. However, drawbacks that those method have limited their application in massive production. Sol-gel method have a relatively long period of production and will involve toxic organ solvent; DNA-directed assembly method is expensive which makes it hard to industrialize; ARM method will break the crystal form of energetic materials and highly depend on the template particles. Besides the many advantages that electrospray method have like easy to setup, high efficiency, monodisperse particle size, etc., our group's previous research shown that particles assembled by electrospray approach have superior combustion performance.[46-48]

3.1. Experiment

Materials

Aluminum nanopowder (~50 nm ALEX, 70 wt% active Al determined by TGA) is purchased from Argonide Corporation. Nitrocellulose (NC) collodion solution (4-8% in ethanol/diethyl ether) is purchased from Sigma-Aldrich and dried in air to get the NC polymers for further use. Copper oxide nanopowder (CuO, ~50 nm), bismuth oxide nanopowder (Bi_2O_3, ~100 nm), tin oxide nanopowder (SnO_2, ~100 nm), tungsten oxide (WO_3, ~100 nm) are purchased from Sigma-Aldrich. Ethanol (200 proof), diethyl ether

(99.0%), dimethylformamide (DMF, 99.8%), acetone (99.8%) are purchased from Sigma Aldrich.

Precursor Preparation

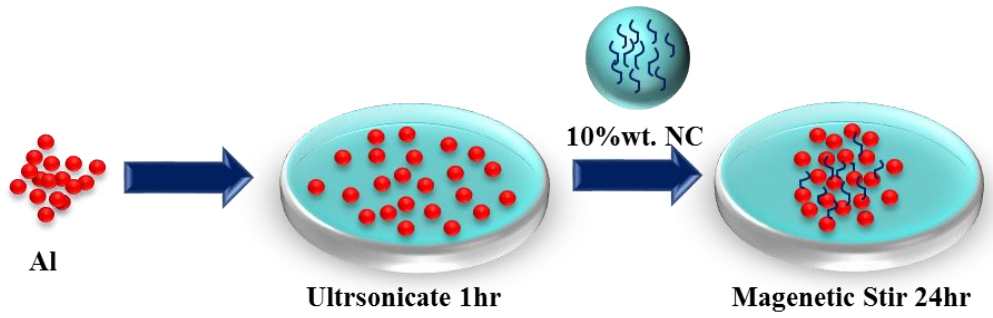

Figure 3.1 Aluminum mesoparticle precursor preparation

For Al mesoparticles, I first weight 185.60 mg Al nanopowder and 14.40 mg Nitrocellulose in the level. Then Al nanopowder is added into a vessel with 1.5 ml ethanol and 0.5 ml diethyl ether mixture(ethanol:ether)=3:1, which has been proved is solvable for Nitrocellulose). Then the precursor is ultrasonicate for 1 hour for homogenous dispersion. After ultrasonication, NC is added in to the system as the binder, then the precursor is put into magnetic stir for 24 hrs. After 24 hours, the precursor is extracted by syringe and ready to electrospray. The typical particle mass loading for Al mesoparticle precursor is 100mg/ml and have a NC content of 10% wt based on the active Al.

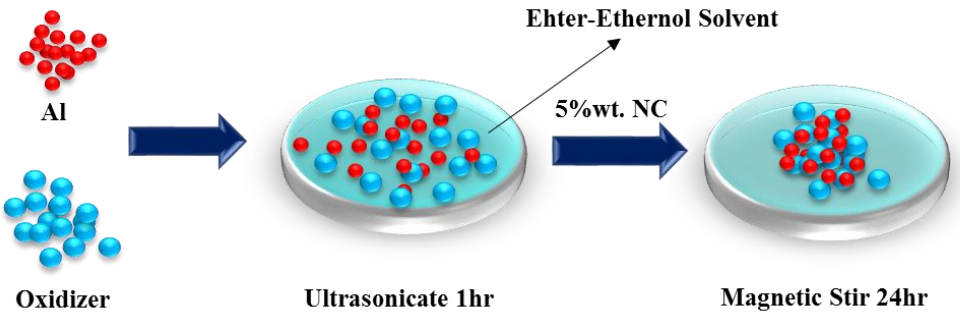

Figure 3.2 Nanothermite precursor preparation

For nanothermite precursor preparation, there are some slightly differences in the precursor preparation process. We take Al/CuO nanothermites as an example.

First, 93.2 mg Al, 288.2 mg CuO and 18.6 mg NC are weight in the level; then, Al and CuO nanopowder are added into solvent (ethanol/ether=3:1) and ultrasonicate for 1 hour to achieve homogenous disperse. After sonification, NC are added into the solvent and the whole system is put into magnetic stir for 24 hours. After 24 hours, the precursor is extracted by syringe and ready to electrospray. The typical particle mass loading for nanothermite precursor is 100mg/ml and have a NC content of 5% wt based on the active Al.

Electrospray Assembly

The typical electrospray setup has been introduced in chapter 2. In this thesis, I use electrospray assembly method to assemble both Al/NC mesoparticles and Al/CuO/NC nanothermites. As seen in fig 3.3, I use syringe pump – syringe system to feed the

precursor into the nozzle. The feed rate of the syringe pump is fixed at 4.5ml/h and a 23 gauge (inner diameter of 0.43 mm) needle is employed. In order to maintain the Tylor-cone jet mode, a 19 kV electrical field is created by two power supply (+10 kV on the needle, -9 kV on the substrate). Also, the distance between needle and substrate is set as 10 cm to give enough time for solvent evaporation.

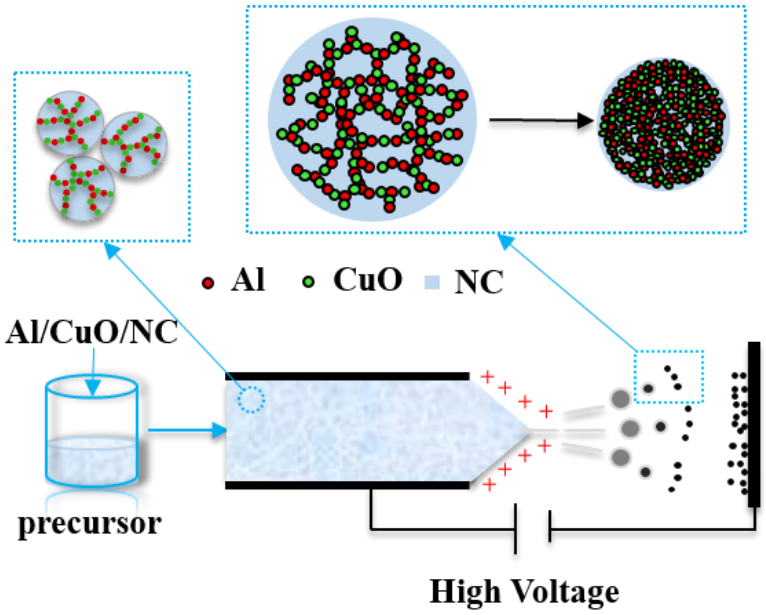

Figure 3.3 Electrospray assembly of Al/CuO/NC nanothermite[47]

When droplet is ejected from the tip of the needle, it will accumulate charge on the surface and interact with the electric field. As the solvent evaporates from the droplet, further charge accumulation will take place. When the charges on the surface reach the Rayleigh limit, the droplet will undergo coulomb fission in order to balance surface tension with electrical force. When the droplet size reaches certain point which electrical force is equal with surface tension, the droplet is stabilized and mesoparticle is formed.

Because the solvent we use has a relatively low saturation pressure, it evaporates fast enough to form hollow sphere particles due to relatively low mass and momentum transfer rate. The mechanism of particle formation will be discussed in detail later.

In this thesis, I will change process variables like solvent (acetone, DMF/ether mixture, etc.), mass loading (25-100 mg/ml), needle size (17G), etc. to study their impact on particle size distribution, morphology and combustion property. The saturation pressure and electrical conductivity data can be found in appendices.

3.2. Results and Discussion

3.2.1 Al/NC mesoparticles

Morphology

From fig 3.4, we can clearly see the difference on the morphology when we change the precursor solvent. Particles generated from ethanol/ether mixture have spherical shape and homogeneous size distribution, which have been confirmed by APS and will be addressed lately. Particles assembled from acetone mixture also have good spherical shape and homogeneous size distribution, as well as porosity which can be found in the TEM image in fig 3.5(b). We propose the difference between ethanol/ether and acetone solvent based mesoparticles result from faster evaporation rate of acetone. The faster solvent evaporation leads to faster particle formation process. With faster particle

formation, the outer shell forms before the solvent inside evaporate completely. After the inner core solvent evaporate, a hollow structure is formed.

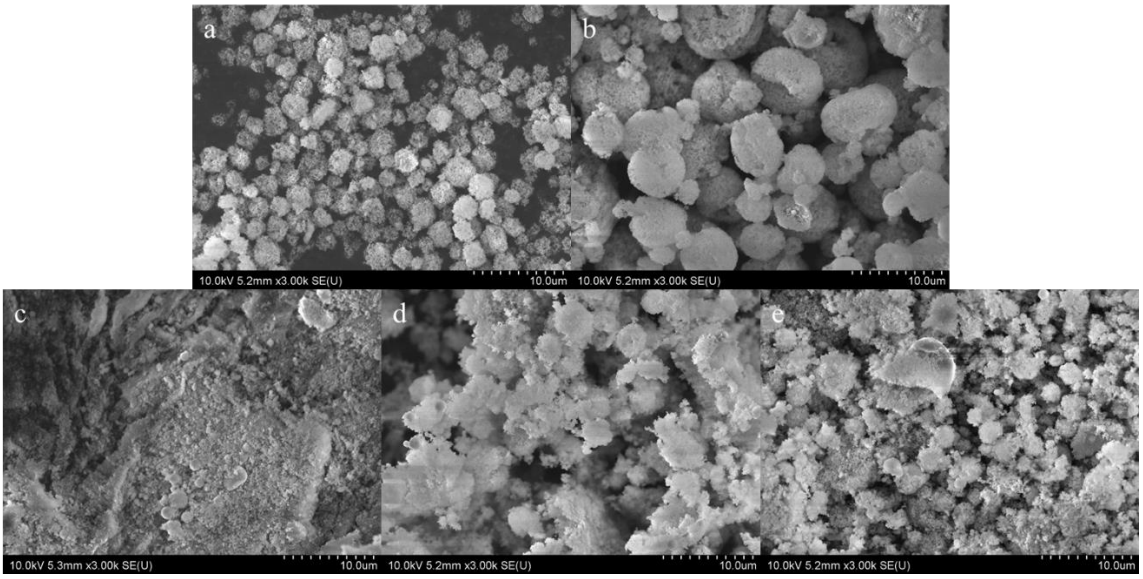

Figure 3.4 SEM images of electrospray assembled Al/NC (10 wt%) mesoparticles based on different solvent. a. ethanol/ether=3:1 mixture; b. Acetone; c. DMF/ether=1:1 mixture; d. DMF/ether=1:2 mixture; e. DMF/ether=1:3 mixture

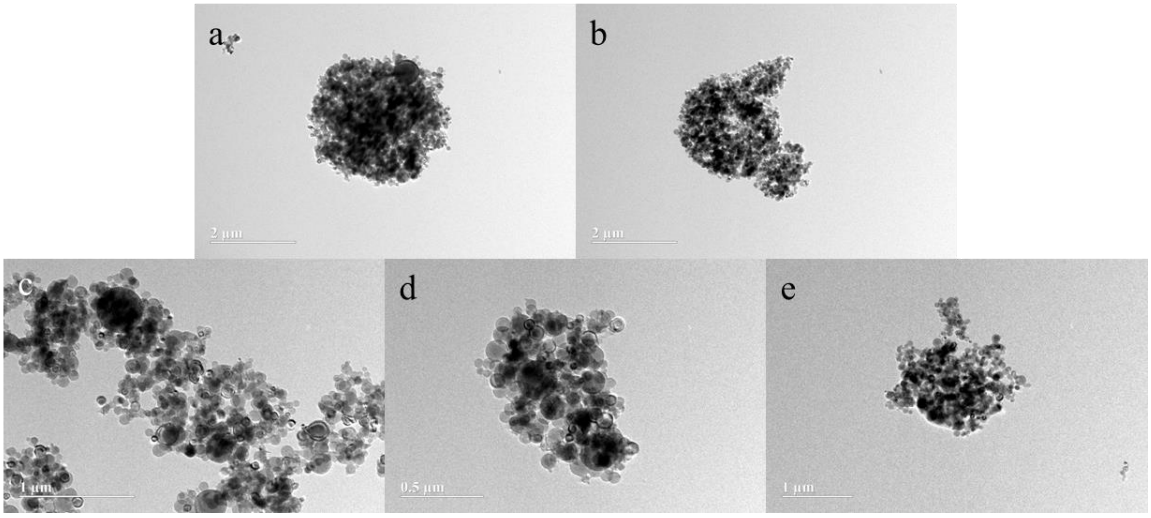

Figure 3.5 TEM images of electrospray assembled Al/NC (10 wt%) mesoparticles based on different solvent. a. ethanol/ether=3:1 mixture; b. Acetone; c. DMF/ether=1:1 mixture; d. DMF/ether=1:2 mixture; e. DMF/ether=1:3 mixture

From c-e in fig 3.4, we can see that particles assembled by different DMF/ether solvent precursor have significant differences on the morphology. As more ether is added into the solvent, the saturation pressure has been increased, which result in fast solvent evaporation. In lower saturation pressure, for example, fig 3.4(c), droplets can not evaporate their solvent compeletely befor they reach the substrate, which result in a wet deposition and thus form film like structure. TEM image in fig 3.5(c-e) also shows that when saturation pressure is increased, more particle like materials are formed.

T-Jump Wire Ignition

The T-jump wire ignition test result is listed in Table 3.1.

Table 3.1 Ignition delay of nano Al and different solvent based Al/NC mesoparticles

Samples	Ignition delay (ms)	Standard deviation
nano Al	15.3	0.57
Ethanol/ether Al/NC	2.9	0.23
Acetone Al/NC	3.6	0.16
DMF/ether=1:1 Al/NC	3.4	0.21
DMF/ether=1:2 Al/NC	2.9	0.12
DMF/ether=1:3 Al/NC	2.4	0.17

From table 3.1, we can see that the ignition delay time varies from different samples. The T-test for each pair of samples can be found in the Appendix C. Nano-sized Al particles have a long ignition delay for 15.3 ms while Al/NC mesoparticle samples have only 2-3 ms of ignition delay time. Combine with previous characterization of morphology (fig 3.4 and 3.5), we can summarize that the morphology differences have a huge impact on the particle ignition process.

The P-value of t-test across each sample are calculated and listed in the Table 3.2. The hypothesis for this t-test is the mean ignition delay time of two samples are same. From the result, the ignition delay time for Al/NC mesoparticle is statistically different with nano-Al particles since the P-value is smaller than the critical P-value (0.05), which indicate we have more than 95% of confident to say that Al/NC mesoparticle have significant difference in ignition delay time compare to Al nanoparticles. More detailed t-test calculation can be found in Appendix C.

Table 3.2 P value of t-test result for each pair of samples.

Samples	Nano Al	Ethanol/ether Al/NC	Acetone Al/NC	DMF/ether =1:1 Al/NC	DMF/ether =1:2 Al/NC	DMF/ether =1:3 Al/NC
Nano Al	1.00	0.00	0.00	0.00	0.00	0.00
Ethanol/ether Al/NC	0.00	1.00	0.06	0.13	0.97	0.15
Acetone Al/NC	0.00	0.06	1.00	0.43	0.03	0.02
DMF/ether=1:1 Al/NC	0.00	0.13	0.43	1.00	0.08	0.03
DMF/ether=1:2 Al/NC	0.00	0.97	0.03	0.08	1.00	0.09
DMF/ether=1:3 Al/NC	0.00	0.15	0.02	0.03	0.09	1.00

Compare between nano-size Al particles and Al/NC mesoparticles, the difference in ignition delay can be a result of the NC content in mesoparticles. NC act as binder and gas generator in the electrospray assembly process. When we heat the Al/NC mesoparticles, NC first decompose and release huge amount of gas due to its low decomposition temperature. Al particle agglomerated will be break into small agglomerate which have higher specific surface area compare to bigger agglomerate and thus lead to faster ignition due to faster heat accumulation.

For different Al/NC mesoparticles, the ignition delay time is also different due to their difference in size and morphology. Acetone based Al/NC mesoparticles have the longer ignition delay time compare to ethanol/ether based Al/NC mesoparticles. As we can see in the SEM and TEM image (fig 3.4 and 3.5), mesoparticles generate from acetone have a porous structure which may lower the heat transfer rate, result in longer ignition delay. Acetone based Al/NC mesoparticles also show significant different ignition delay time compare to nano-Al particles, however, P-value of Ethanol/ether based and acetone based particles indicate the change in ignition time is not significant different due to $P>0.05$.

DMF/ether samples show that as the ratio of ether increased, the ignition delay time reduced from 3.4 to 2.4 ms, which indicate that the sphere like structure is favorable for combustion due to higher pack density of particles. The higher ether ratio also increase the saturation pressure of the precursor thus lead to more particles generated instead of film. The heat accumulation inside a 3D sphere structure is faster than a 2D film structure

as spherical structure have larger specific surface area. For DMF/ether based particles, both samples with DMF/ether ratio of 1:2 and 1:3 have P value falls in the confidence interval, which indicate that as more ether is added into the precursor system, the mesoparticles they generate have significant different in ignition delay time compare to 1:1 ratio sample. However, the ignition delay time difference between 1:2 and 1:3 DMF/ether ratio sample is not significant. This phenomenon possibly indicate that as the saturation pressure increased, decrease of ignition delay time become less significant since more spherical particles are formed which is favorable for combustion process.

3.2.2 Al/oxidizer/NC nanothermites

Morphology

From the SEM images in fig 3.6, we can see the difference between nanothermites synthesized by different precursor solvent. The NC content in the formula works as the binder to bind the Al and oxidizer particle closely, which improves their combustion property. By using acetone as the solvent, both Al/CuO nanothermite and Al/Bi_2O_3 nanothermite show more sphere like structures than ethanol/ether based sample in the SEM. This phenomenon is result from acetone's higher saturation pressure and surface tension which allow droplet to maintain more sphere like shape in the electric field.

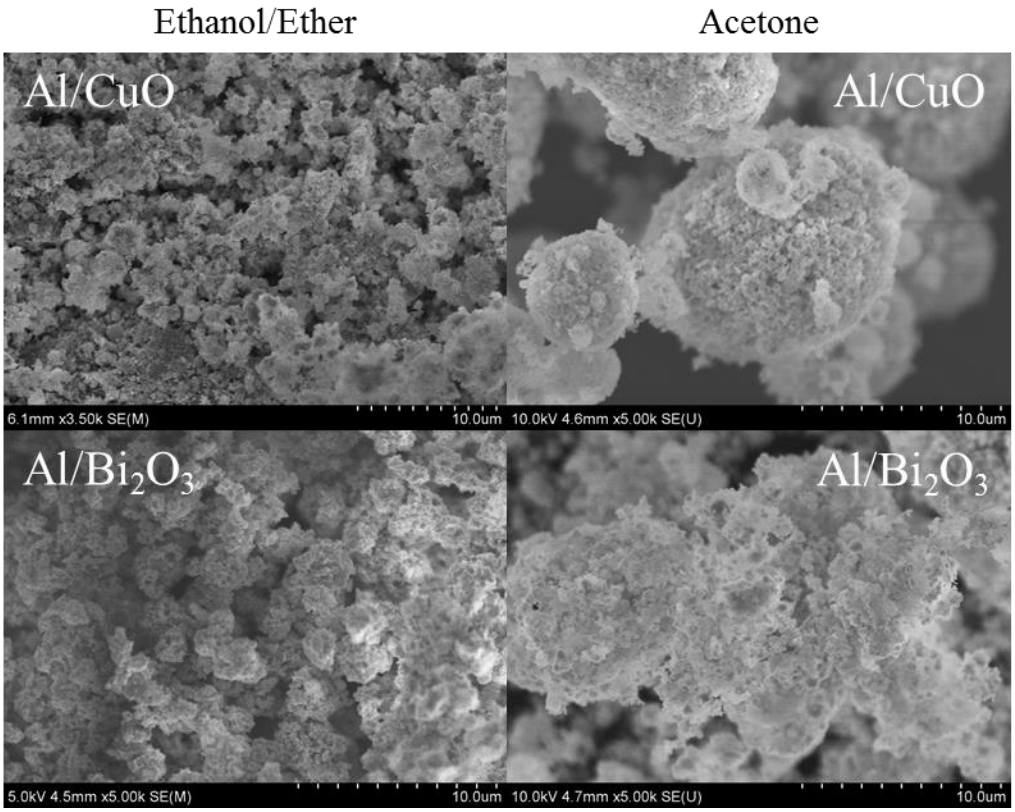

Figure 3.6 SEM image of ethanol/ether based electrospray nanothermite (left) and acetone based electrospray nanothermite (right)

Pressure cell measurement

The test result of Al/CuO/NC and Al/Bi_2O_3/NC nanothermite in the table 3.3 shows that nanothermite synthesized from acetone precursor have higher pressurization rate and shorter burn time. By using acetone as the precursor solvent, the pressurization rate has been improved by 39.0% and 99.9% for Al/CuO and Al/Bi_2O_3, as well as reduce 23.1% and 25.9% in burn time.

Table 3.3 Pressure cell test result of ethanol/ether based and acetone based nanothermite

Composite	Max Pressure (Kpa)	Pressurization Rate (KPa/ms)	FWHM Burn Time (ms)
Al/CuO-Ethanol/ether	1450.	36274	0.27
Al/CuO-Acetone	1411	50420	0.21
Al/Bi2O3-Ethanol/ether	1281	33712	0.51
Al/Bi2O3-Acetone	1078	67402	0.37

This phenomenon indicate that the difference in morphology actually affect the combustion performance of nanothermite we synthesize. From the SEM image of these two kind of nanothermite samples, we can see that samples using acetone as the precursor solvent have tighter structure compare to samples using ethanol/ether. This structure difference leads to more intimate contact for Al and oxidizer particles in acetone based samples. The mass and heat transfer is enhance in acetone based samples which result in faster and more efficient combustion.

Chapter 4: Design and Manufacture of Electrospray Mesoparticle Generator and *In-Situ* Measurement

In this chapter, an electrospray mesoparticle generator is introduced and described in detail. With the help of this mesoparticle generator, we are able to tune the properties of particles as well as test them *in-situ*.

4.1 Design and manufacture of electrospray mesoparticle generator.

Typical setup of electrospray has its limitation on the characterization, such like size distribution and combustion property measurement. Previously, we need to first electrospray assemble those mesoparticles and collected them from the substrate. After we have the particles, we need to take them to SEM and manually measure and count particle size to get the size distribution, which is not very accurate. For burn time measurement, we need to use particle aerosolizer to flow mesoparticles inside the burner to get the burn time and speed.

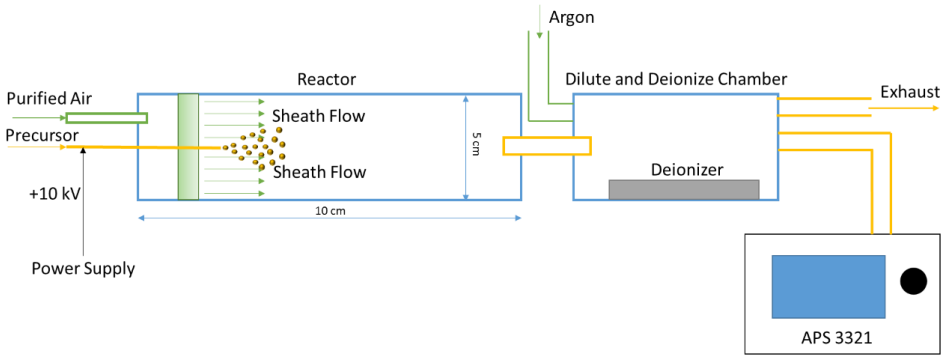

Figure 4.1 Schematics of electrospray mesoparticle generator

In order to deal with this limitation and conduct particle property measurements *in-situ*, I design and manufacture a mesoparticle generator as illustrate in fig 4.1. In this setup, I still use the syringe pump – syringe system as the feed for precursor. Alternatively, a longer needle, 1.5 inches long, will be used in order to get into the reactor chamber for electrospray. The reactor chamber is made of a 10 cm long glass tube with 50 mm outer diameter and 46mm inner diameter. At two ends of the tube, two flange to quick connect coupling adapter is applied to seal the chamber. Three air inlet is applied on the left side coupling adapter in order to supply carrier gas (filtered air, 5L/min). Also, a hole is drilled on the left side coupling adapter to let the needle go through the adapter and inside the chamber.

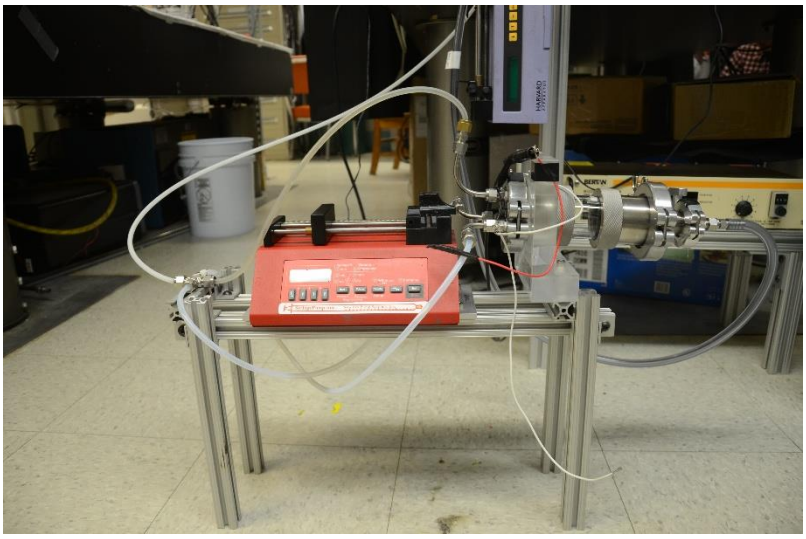

Figure 4.2 Picture of electrospray mesoparticle generator setup

Typically, a deionizer (Po_210, 500 μCi source) is inserted at the end of the reactor chamber in order to neutralize the particle charge and minimize particle loss along the tube during the combustion property measurement. For particle size distribution test, we

need another dilution chamber in order to lower the particle number concentration to obtain higher accuracy and protect APS from excessive concentration of particles. The dilute chamber is made of a glass tube which have two rubber stoppers on each side of the tube. Argon is flowed into the dilute chamber at the left along with the aerosol and then the aerosol is sucked into the APS by the rate of 5L/min. Extra gases is vented through the exhaust port at the right of dilute chamber.

4.2 *In-situ* particle size distribution measurement

4.2.1 Experiment

For particle size distribution measurement, we first take the precursor into a 10ml syringe with 23G (17G) needle, then the syringe is put on the syringe pump and the needle is connected with power supply. Then feed rate is set as 4.5ml/hr which has been calibrated based on the diameter of syringe. Because the APS test the particle by inhale aerosol, filtered air is set at a flow rate of 5L/hr in order to fit the need of APS. A positive 10kV voltage is added at the needle to create electric field for electrospray.

By using APS, we can directly control the test process and receive data on laptop. The raw data will be calculated and fit into lognormal distribution model to get the mean particle size and distribution.

4.2.2 Result and Discussion

Precursor mass loading

From fig 4.3, we can see that as the precursor mass loading increase, the particle mean size and standard deviation increases only slightly. The mean size and standard deviation data is listed in table 4.1

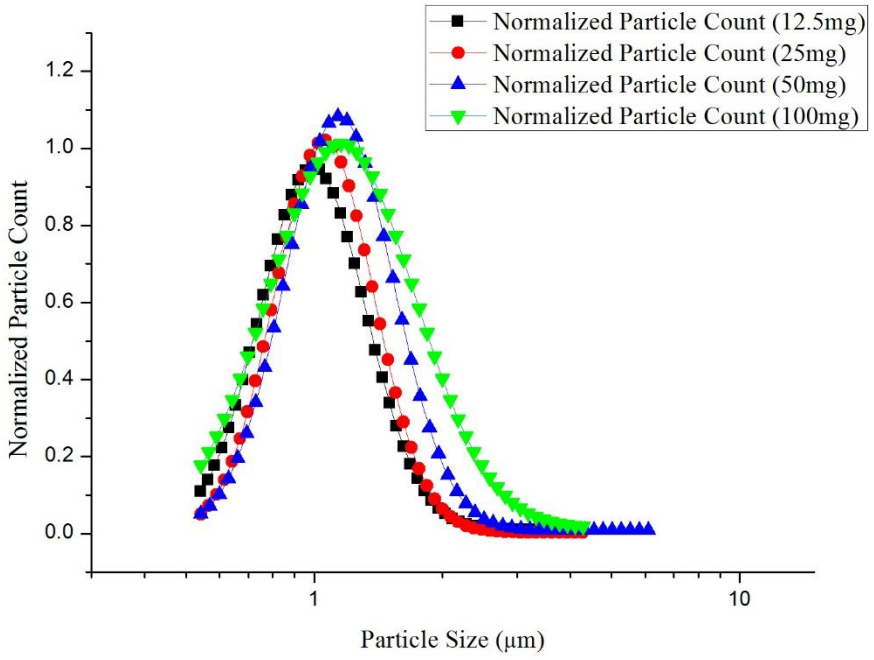

Figure 4.3 lognormal fit particle size distribution of different precursor mass loading

The reason for this phenomenon we proposed is that when precursor have higher mass loading, the initial droplet have more nano Al particles inside. As the solvent evaporate, the mesoparticle assembled in higher mass loading tend to contain more nanoparticles, thus can create larger particles. Also, more particle in the droplet means higher electric

conductivity for the droplet, the charge are easier accumulate on the surface of droplet and induce Coulomb fission. The wider size distribution is a result of Coulomb fission effect since more particles are undergo fission process.

Table 4.1(a) Mean size and standard deviation for different precursor mass loadings

Mass loading(mg/ml)	Mean size (μm)	Standard deviation
12.5	1.08	0.28
25	1.13	0.27
50	1.25	0.29
100	1.38	0.41

I calculate the theoretical droplet size for the particle with different mass loadings and the result is listed in the table below. In this calculation we assume the particle shape to be spherical and the void fraction is 0.65, based on previous research. [53] Theoretical droplet diameter is calculated based on the mass balance between droplet and precursor mass loading, which can be seen in below.

$$(1-\phi)\times\frac{4}{3}\pi(d_{particle}/2)^3\times\rho_{Al}=\rho_{precursor}\times\frac{4}{3}\pi(d_{droplet}/2)^3$$

In this equation, ϕ is the void fraction of mesoparticles; ρ_{Al}, $\rho_{precursor}$ are density of aluminum and mass loading of precursor; $d_{particle}$ and $d_{droplet}$ are the diameters of mesoparticles and droplets.

Table 4.1(b) Droplet diameter for different precursor mass loadings

Mass loading (mg/ml)	droplet diameter (μm)
12.5	4.6
25	3.8
50	3.3
100	2.9

As we can see from the table 4.1(b), the theoretical droplet diameter decreases as the mass loading increase, which shows that as the particle loading increase, the electrical conductivity is likely increasing and thus lowering the Rayleigh limit to form smaller droplets due to the equilibrium of electrical force and surface tension.

Needle size

From fig 4.4 we can see that the particle size distribution for different needle size can be describe as the particle mean size and standard deviation for ethanol/ether mixture solvent is slightly increased as the needle size increase. For Acetone solvent, the mean particle size and standard deviation show no clear difference. The more detailed data can be found in table 4.2

Table 4.2 Mean size and standard deviation for different needle size

Experiment	mean size	standard deviation
Ethanol/ether 23G	1.4	0.51
Ethanol/ether 17G	2.0	0.59
Acetone 23G	0.73	0.26
Acetone 17G	0.76	0.26

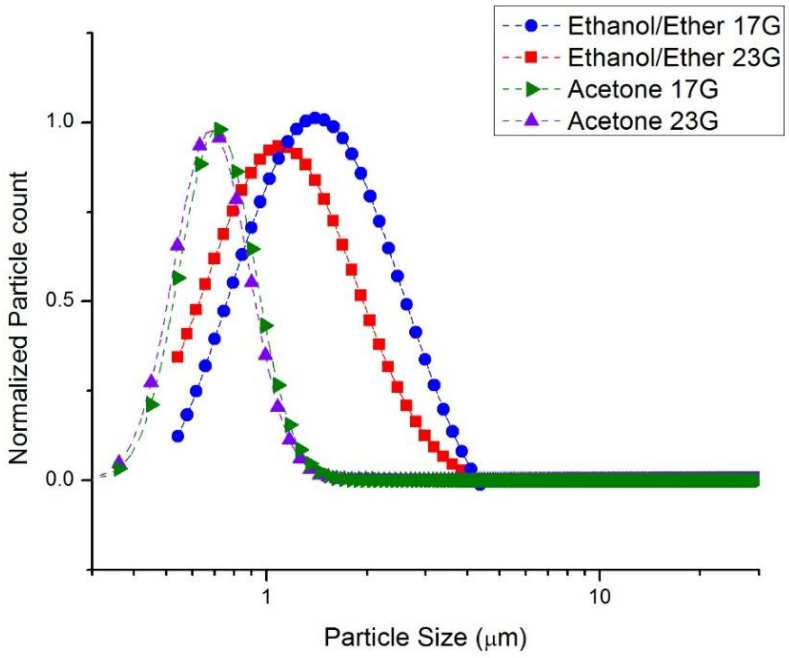

Figure 4.4 Lognormal fit particle size distribution for different needle size and precursor solvent.

This phenomenon is result from the bigger needle diameter. Needle with bigger diameter will have a bigger meniscus at the tip which leads to bigger initial droplet size. The bigger initial droplet will have more nanoparticles inside and when the droplet undergo Coulomb fission, it will have more particles in the offspring droplet.

The reason why particles generated from acetone precursor have almost the same size distribution can be explained as the acetone have higher electric conductivity and thus the charge accumulation process is faster than ethanol/ether solvent. The droplet reaches the same equilibrium for both condition during the solvent evaporation process and the final

droplet size before total evaporation is the same, thus give the particles the same size distribution for both case. From the SEM images (fig 4.5), we can also see that the size and morphology are almost identical for this two kind of mesoparticles.

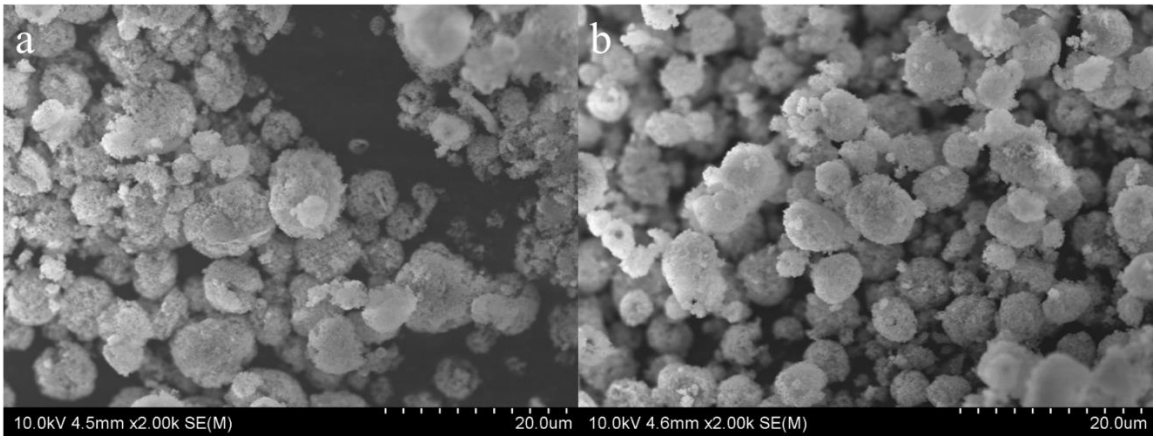

Figure 4.5 SEM images of different needle size electrospray acetone solvent Al/NC mesoparticles. a. 23 gauge b. 17 gauge

Precursor solvent

From the above image (fig 4.6), we can see that there is difference in particle size distribution between different types of precursor solvent we choose. Ethanol/ether based mesoparticles have the biggest mean particle size and widest particle size distribution. Acetone based mesoparticles have smaller size and narrower size distribution than ethanol/ether. DMF/ether based mesoparticles have almost the same mean size and standard deviation, however, as more ether is added into the solvent, slightly wider distribution can be observed. More detailed data can be found in table 4.3.

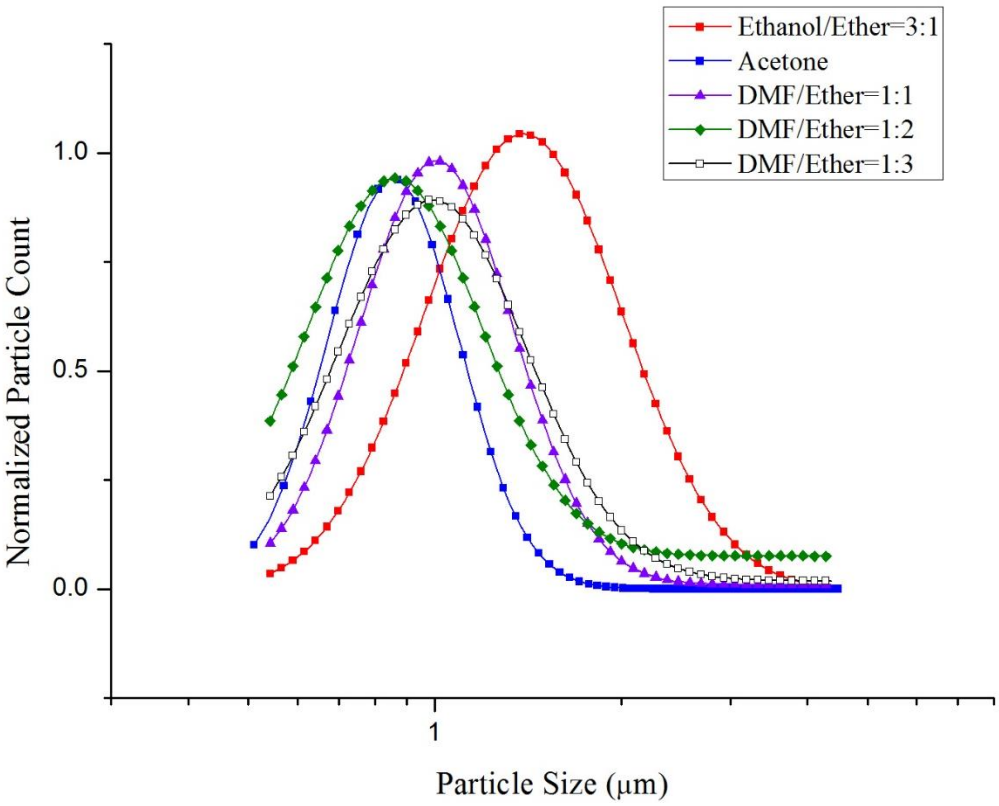

Figure 4.6 Lognormal fit particle size distribution for different precursor solvent

The reason for this particle size distribution difference can be describe as the following: for ethanol/ether and acetone, acetone have higher saturation pressure which means faster solvent evaporation and faster fission process, less nano Al particles will be contained in each droplet. Thus, the mean size of acetone based mesoparticle is smaller than ethanol/ether based mesoparticle. The reason why ethanol/ether based mesoparticles have higher standard deviation can be explained as ethanol/ether solvent have lower Rayleigh limit which allows more Coulomb fission during the solvent evaporation process and result in more offspring particle with different size.

Table 4.3 Mean size and standard deviation for different needle size

Experiment	mean size	standard deviation
Ethanol/ether	1.59	0.37
Acetone	0.91	0.24
DMF/ether=1:1	0.84	0.19
DMF/ether=1:2	0.77	0.21
DMF/ether=1:3	0.85	0.23

For DMF/ether based mesoparticle, the higher ratio of ether results in higher saturation pressure which increases the solvent evaporation rate. From fig 3.4 and fig 3.5 in chapter 3, we can clearly see that more particles are formed in higher ether concentration samples, which suggest more Coulomb fission is taken place in that higher ether concentration sample. The very narrow size distribution is result of the polymer entanglement in lower saturation pressure samples. The entanglement effect allows particle combine with other particle below the Rayleigh limit and suppress Coulomb fission effect, thus form more homogenous particles. However, we should notice that in DMF/ether=1:1 and 1:2 samples, very few particles are formed compare to ethanol/ether and acetone samples.

4.3 *In-situ* combustion time measurement

4.3.1 Experiment

In the combustion speed measurement, using the electrospray particle generator to assemble Al/NC mesoparticles and using filtered gas to send them into the burner. In this measurement, we use lower flow rate for carrier gas as 1.5L/min and the diluter chamber is absent since we want to maximize particle concentration in the aerosol.

The typical flame in the burn can be seen in fig 4.7, which we can clearly see that in the core of the flame there is a bright stream of burning particles. The gas we use in this burner is mixture of oxygen/methane/nitrogen. Mesoparticles assembled from the generator are carried into the center of the flame by carrier gas and burn. The whole burning process is recorded by high speed camera and analyzed by the phantom camera software.

Figure 4.7 Picture of Al/NC flame for in-situ combustion speed measurement

The flame temperature profile for different gas composition is measured by platinum thermal couple and result is shown in fig 4.8. As we seen in fig 4.8, the temperature along the height of the flame has a narrow range less than 200 degree, so we can assume this burning process is isothermal, which gives us advantage on analyze the combustion property of Al/NC mesoparticles.

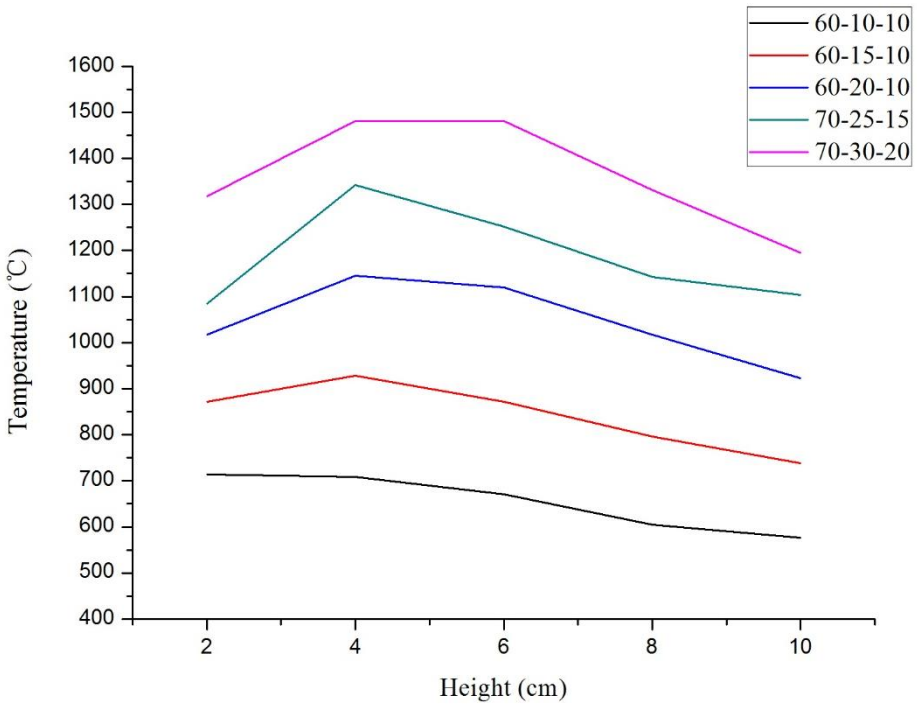

Fig 4.8 Temperature profile for different oxygen/methane/nitrogen ratio

4.3.2 Result and Discussion

The result of Al nanoparticles and Al/NC mesoparticles burn time measurement is presented in fig 4.9. We can see that the average burn time for Al/NC mesoparticles (366 μs) are much shorter than Al nanoparticles (4063 μs) in flame with gas ratio of 60-8-10. Also, the burn time distribution of Al/NC mesoparticles is much narrower than Al nanoparticles.

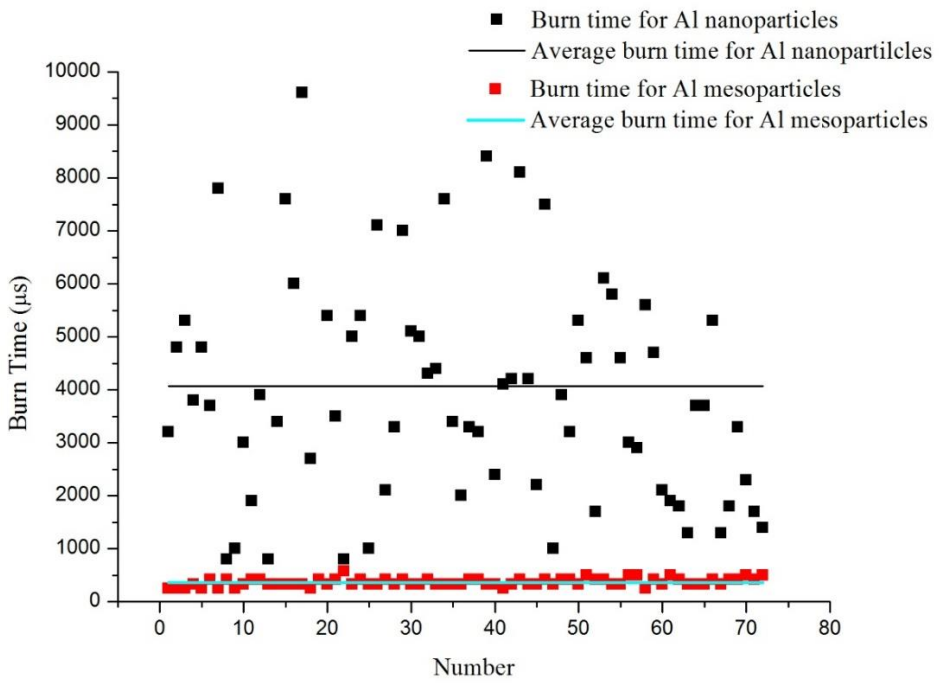

Fig. 4.9 Burn time profile for Al nanoparticles and Al/NC mesoparticles

The mechanism we propose for Al/NC mesoparticle combustion can be summarized as the NC polymer we added into the mesoparticle act as not only binder but also gas generator. When we heat the mesoparticles, NC will release gas and break the mesoparticle into small agglomerates which have larger specific surface area compare to bigger Al agglomerate. In the contrary, Al nanoparticle usually forms large agglomerate which will sinter into huge spherical particle when it is heated, thus result in much slower heat accumulation compare to the mesoparticles.

Chapter 5: Summary and Future Direction

5.1 Conclusion

Energetic material, especially for Al-based energetic material, has various application in explosives, propellants and pyrotechnics. By using electrospray, we are able to assemble Al-based energetic mesoparticles with controllable size and morphology. The combustion performance of these mesoparticles are greatly improved due to faster inward mass and heat diffusion which result from more intimate particle contact and polymer insulation effect.

From the experiments and results we presented in this thesis, we have studied the various variables like needle size, precursor solvent, mass loading, etc. and their impact on the electrospray assemble process. We successfully design and manufactured an electrospray mesoparticle generator which allows us to conduct in-situ measurement on size distribution and burn time. Compare to Al nanoparticles and conventional Al/Oxidizer thermite, the mesoparticles we synthesized have controllable size and morphology as well as shorter ignition delay and more efficient combustion.

5.2 Future direction

5.2.1 Improved Al-based mesoparticle synthesis and characterization

From the work our group have done, we have conduct intense study on Al-based mesoparticle from synthesis to post-experiment combustion characterization. Further work on Al/NC mesoparticles are still needed since aluminum particle is an important fuel source in various application. There are two major area we can further explore on, which is synthesize Al-based mesoparticle with tunable morphology and size, investigate on the mechanism of aluminum-based mesoparticle ignition and combustion under different atmosphere still need further study.

For the synthesis part, we can try to change the conductivity of the precursor system by adding salt or other conductive additives. The conductivity change on the precursor should have huge impact on the morphology and size because it can affect the charge accumulation process on the sprayed droplet. Currently, we can only change the mean size of Al/NC mesoparticle a little bit (1-2 μm), if we can change the mean size to a bigger scale by changing conductivity or other variable, we can more thoroughly understand the mechanism of mesoparticle assembly in electrospray and provide valuable source for further combustion measurement.

For the post-experiment characterization part, we currently burning the samples in oxygen/methane/nitrogen flame. In the future, we can work on incorporate the mesoparticle generator with other test instrument like combustion which allows us to ignite and burn mesoparticles in other atmosphere, for instance, oxygen, argon, etc. This will help us better understand the mechanism of mesoparticle ignition and combustion.

5.2.2 Modified electrospray mesoparticle generator

Our current experiment based on the mesoparticle generator are limited to Al/NC mesoparticle due to the safety issue. In the future, we can modify the mesoparticle generator to make it suitable for produce other kind of mesoparticles like nanothermite as well as test them in the combustion measurement.

Possible modification include upgrade for a thicker glass tube as the reactor chamber; add pressure release value in case of nanothermite explosion. These upgrades should provide us the safety requirement on assemble nanothermite inside the mesoparticle generator and gives us another way to test nanothermites' combustion performance

Appendices

Appendix A. Saturation pressure for different components

The saturation pressure is calculated by Antonin equation which is listed below:

$$\log_{10}(P) = A - (B/(T+C))$$

The coefficient of each component is obtained from the webbook of NIST[54], and the saturation pressure is listed in Table A1:

Table A1. Saturation Pressure for pure components

Substance	Saturation Pressure (KPa)
Ethanol	5.85
Diethyl Ether	58.89
Acetone	25.09
DMF	0.38

In order to get the saturation pressure of the binary mixture, we assume the mixture is ideal and the saturation pressure of each mixture is calculated by Raoult's law:

$$P_{total} = P_A \times x_A + P_B \times x_B$$

P_A, P_B are saturation pressure for pure component A and B; x_A, x_B are molar fraction of each component.

The calculated result of saturation pressure is listed in the table A2.

Table A2. Saturation Pressure for different precursor solvent

Substance	Saturation Pressure (KPa)
Ethanol/Ether=3:1	14.22
Acetone	25.09
DMF/Ether=1:1	25.31
DMF/Ether=1:2	35.34
DMF/Ether=1:3	40.76

Appendix B. Electrical conductivity of different components

The electrical conductivity data of pure substance is obtained from the handbook.[55]

Table B1. Electrical conductivity for pure substance

Substance	Electrical Conductivity (S/cm)
Ethanol	1.40E-09
Diethyl Ether	3.00E-16
Acetone	5.00E-09
DMF	6.00E-08

In this thesis, we choose the ideal mixture serials model to calculate electrical conductivity of mixture in order to get the mixture conductivity. In this case, we treat the mixture system as a series connection of resistance.

The relationship between electrical conductivity (σ) and resistance (ρ) can be illustrated as:

$$\rho = 1/\sigma$$

The total resistance of mixture is:

$$\rho_{total} = \rho_A \times x_A + \rho_B \times x_B$$

ρ_A, ρ_B are saturation pressure for pure component A and B; x_A, x_B are molar fraction of each component. Calculated data for electrical conductivity is listed in Table B2.

Table B2. Electrical conductivity for different precursor solvent

Substance	Electrical Conductivity (S/cm)
Ethanol/Ether=3:1	1.90E-16
Acetone	5.00E-9
DMF/Ether=1:1	7.04E-16
DMF/Ether=1:2	5.02E-16
DMF/Ether=1:3	4.35E-16

Appendix C. T-test of Ignition delay test results

For the t-test of the ignition delay, we choose two tailed distribution for two equal variance samples as the test method. The equation I use is listed below:

$$t = \frac{\overline{X_1} - \overline{X_2}}{\sqrt{\frac{(n_1 - 1)s^2_{X1} + (n_2 - 1)s^2_{X2}}{n_1 + n_2 - 2} \times (\frac{1}{n_1} + \frac{1}{n_2})}}$$

In this equation, X, s^2 and n are the mean, variance and size of the sample.

After the t value is get, we can use t value combine with the degree of freedom to get the P value for each pair of samples. Common critical P value is set as 0.05 which indicate when P is greater than 0.05, there is no significant difference between two samples.

Reference

1 Wang, H., Jian, G., Yan, S., DeLisio, J. B., Huang, C., & Zachariah, M. R. (2013). Electrospray formation of gelled nano-aluminum microspheres with superior reactivity. ACS applied materials & interfaces, 5(15), 6797-6801.

2 Rossi, C., Zhang, K., Esteve, D., Alphonse, P., Tailhades, P., & Vahlas, C. (2007). Nanoenergetic materials for MEMS: A review. *Journal of Microelectromechanical Systems, 16*(4), 919-931.

3 Weismiller, M. R., Malchi, J. Y., Yetter, R. A., & Foley, T. J. (2009). Dependence of flame propagation on pressure and pressurizing gas for an Al/CuO nanoscale thermite. *Proceedings of the Combustion Institute, 32*, 1895-1903.

4 Yen, N. H., & Wang, L. Y. (2012). Reactive Metals in Explosives. *Propellants Explosives Pyrotechnics, 37*(2), 143-155.

5 Agrawal, J. P. (1998). Recent trends in high-energy materials. *Progress in Energy and Combustion Science, 24*(1), 1-30.

6 Badgujar, D. M., Talawar, M. B., Asthana, S. N., & Mahulikar, P. P. (2008). Advances in science and technology of modern energetic materials: An overview. *Journal of Hazardous Materials, 151*(2-3), 289-305.

7 Brill, T. B., & James, K. J. (1993). Kinetics and mechanisms of thermal decomposition of nitroaromatic explosives. *Chemical reviews, 93*(8), 2667-2692.

8 Rozenband, V. I., & Vaganova, N. I. (1992). A Strength Model of Heterogeneous Ignition of Metal Particles. *Combustion and Flame, 88*(1), 113-118.

9 Trunov, M. A., Schoenitz, M., & Dreizin, E. L. (2006). Effect of polymorphic phase transformations in alumina layer on ignition of aluminium particles. *Combustion Theory And Modelling, 10*(4), 603-623.

10 Kazakov, Y. V., Medvedev, A., Fedorov, A., & Fomin, V. (1987). Mathematical modelling of ignition in dusty gases. *Arch. Combust., 7*(1), 7-17.

11 Dreizin, E. L. (2009). Metal-based reactive nanomaterials. *Progress in Energy and Combustion Science, 35*(2), 141-167.

12 Babuk, V. A., & Vasilyev, V. A. (2002). Model of aluminum agglomerate evolution in combustion products of solid rocket propellant. *Journal of Propulsion And Power, 18*(4), 814-823.

13 Kwon, Y. S., Jung, Y. H., Yavorovsky, N. A., Illyn, A. P., & Kim, J. S. (2001). Ultra-fine powder by wire explosion method. *Scripta Materialia, 44*(8-9), 2247-2251.

14 Sarathi, R., Sindhu, T. K., & Chakravarthy, S. R. (2007). Generation of nano aluminium powder through wire explosion process and its characterization. *Materials Characterization, 58*(2), 148-155.

15 Sarathi, R., Sankar, B., & Chakravarthy, S. R. (2010). Influence of Nano Aluminium Powder Produced by Wire Explosion Process at Different Ambience on Hydrogen Generation. *Journal of Electrical Engineering-Elektrotechnicky Casopis, 61*(4), 215-221.

16 Dreizin, E. L. (2003). Effect of phase changes on metal-particle combustion processes. *Combustion Explosion and Shock Waves*, *39*(6), 681-693.

17 Jian, G. Q., Chowdhury, S., Sullivan, K., & Zachariah, M. R. (2013). Nanothermite reactions: Is gas phase oxygen generation from the oxygen carrier an essential prerequisite to ignition? *Combustion and Flame*, *160*(2), 432-437.

18 Sullivan, K., Young, G., & Zachariah, M. R. (2009). Enhanced reactivity of nano-B/Al/CuO MIC's. *Combustion and Flame*, *156*(2), 302-309.

19 Jacob, R. J., Jian, G. Q., Guerieri, P. M., & Zachariah, M. R. (2015). Energy release pathways in nanothermites follow through the condensed state. *Combustion and Flame*, *162*(1), 258-264.

20 Piekiel, N. W., Zhou, L., Sullivan, K. T., Chowdhury, S., Egan, G. C., & Zachariah, M. R. (2014). Initiation and reaction in Al/Bi2O3 nanothermites: evidence for the predominance of condensed phase chemistry. *Combustion Science and Technology*, *186*(9), 1209-1224.

21 Rayleigh, L. (1882). XX. On the equilibrium of liquid conducting masses charged with electricity. *Philosophical Magazine Series 5*, *14*(87), 184-186.

22 Almer á, B., Deng, W., Fahmy, T. M., & Gomez, A. (2010). Controlling the morphology of electrospray-generated PLGA microparticles for drug delivery. *Journal of Colloid and Interface Science*, *343*(1), 125-133.

23 Gomez, A., & Tang, K. (1994). Charge and fission of droplets in electrostatic sprays. *Physics of Fluids (1994-present), 6*(1), 404-414.

24 Jaworek, A., & Sobczyk, A. T. (2008). Electrospraying route to nanotechnology: An overview. *Journal of Electrostatics, 66*(3-4), 197-219.

25 Ganan-Calvo, A. M., Lasheras, J. C., Davila, J., & Barrero, A. (1994). The Electrostatic Spray Emitted From an Electrified Conical Meniscus. *Journal of Aerosol Science, 25*(6), 1121-&.

26 Ganan-Calvo, A. M., Davila, J., & Barrero, A. (1997). Current and droplet size in the electrospraying of liquids. Scaling laws. *Journal of Aerosol Science, 28*(2), 249-275.

27 Salata, O. V. (2005). Tools of nanotechnology: Electrospray. *Current Nanoscience, 1*(1), 25-33.

28 Taylor, G. (1964). *Disintegration of water drops in an electric field.* Paper presented at the Proceedings of the Royal Society of London A: Mathematical, Physical and Engineering Sciences.

29 Cloupeau, M., & Prunet-Foch, B. (1994). Electrohydrodynamic spraying functioning modes: a critical review. *Journal of Aerosol Science, 25*(6), 1021-1036.

30 Cloupeau, M., & Prunetfoch, B. (1989). Electrostatic Spraying Of Liquids in Cone-Jet Mode. *Journal of Electrostatics, 22*(2), 135-159.

31 Cloupeau, M., & Prunetfoch, B. (1990). Electrostatic Spraying Of Liquids - Main Functioning Modes. *Journal of Electrostatics, 25*(2), 165-184.

32 Jaworek, A., & Krupa, A. (1999). Classification of the modes of EHD spraying. *Journal of Aerosol Science, 30*(7), 873-893.

33 Shiryaeva, S., & Grigor'ev, A. (1995). The semiphenomenological classification of the modes of electrostatic dispersion of liquids. *Journal of ELECTROSTATICS, 34*(1), 51-59.

34 Wilhelm, O., Mädler, L., & Pratsinis, S. E. (2003). Electrospray evaporation and deposition. *Journal of Aerosol Science*, *34*(7), 815-836.

35 Rosell-Llompart, J., & De La Mora, J. F. (1994). Generation of monodisperse droplets 0.3 to 4 μm in diameter from electrified cone-jets of highly conducting and viscous liquids. *Journal of Aerosol Science, 25*(6), 1093-1119.

36 Swarbrick, J. C., Taylor, J. B., & O'Shea, J. N. (2006). Electrospray deposition in vacuum. *Applied surface science, 252*(15), 5622-5626.

37 Jaworek, A. (2007). Micro- and nanoparticle production by electrospraying. *Powder Technology, 176*(1), 18-35.

38 Xu, Y., & Hanna, M. A. (2007). Electrosprayed bovine serum albumin-loaded tripolyphosphate cross-linked chitosan capsules: synthesis and characterization. *Journal of microencapsulation, 24*(2), 143-151.

39 Xu, Y., Skotak, M., & Hanna, M. (2006). Electrospray encapsulation of water-soluble protein with polylactide. I. Effects of formulations and process on morphology and particle size. *Journal of microencapsulation, 23*(1), 69-78.

40 Kenawy, E.-R., Bowlin, G. L., Mansfield, K., Layman, J., Simpson, D. G., Sanders, E. H., et al. (2002). Release of tetracycline hydrochloride from electrospun poly (ethylene-co-vinylacetate), poly (lactic acid), and a blend. *Journal of controlled release, 81*(1), 57-64.

41 Bölgen, N., Vargel, I., Korkusuz, P., Menceloğlu, Y. Z., & Pişkin, E. (2007). In vivo performance of antibiotic embedded electrospun PCL membranes for prevention of abdominal adhesions. *Journal of Biomedical Materials Research Part B: Applied Biomaterials, 81*(2), 530-543.

42 Kim, K., Luu, Y. K., Chang, C., Fang, D., Hsiao, B. S., Chu, B., et al. (2004). Incorporation and controlled release of a hydrophilic antibiotic using poly (lactide-co-glycolide)-based electrospun nanofibrous scaffolds. *Journal of Controlled Release, 98*(1), 47-56

43 Xu, X., Chen, X., Xu, X., Lu, T., Wang, X., Yang, L., et al. (2006). BCNU-loaded PEG–PLLA ultrafine fibers and their in vitro antitumor activity against Glioma C6 cells. *Journal of Controlled Release, 114*(3), 307-316.

44 Liang, D., Luu, Y. K., Kim, K., Hsiao, B. S., Hadjiargyrou, M., & Chu, B. (2005). In vitro non-viral gene delivery with nanofibrous scaffolds. *Nucleic acids research, 33*(19), e170-e170.

45 Nasir, M., Matsumoto, H., Danno, T., Minagawa, M., Irisawa, T., Shioya, M., et al. (2006). Control of diameter, morphology, and structure of PVDF nanofiber fabricated by

electrospray deposition. *Journal of Polymer Science Part B: Polymer Physics, 44*(5), 779-786.

46 Yan, S., Jian, G., & Zachariah, M. R. (2012). Electrospun nanofiber-based thermite textiles and their reactive properties. *ACS applied materials & interfaces, 4*(12), 6432-6435.

47 Wang, H., Jian, G., Egan, G. C., & Zachariah, M. R. (2014). Assembly and reactive properties of Al/CuO based nanothermite microparticles. *Combustion and Flame, 161*(8), 2203-2208.

48 Huang, C., Jian, G., DeLisio, J. B., Wang, H., & Zachariah, M. R. (2015). Electrospray Deposition of Energetic Polymer Nanocomposites with High Mass Particle Loadings: A Prelude to 3D Printing of Rocket Motors. *Advanced Engineering Materials, 17*(1), 95-101.

49 Aerodynamic Particle Sizer (APS) Spectrometer 3321. (n.d.). Retrieved March 23, 2015, from http://www.tsi.com/aerodynamic-particle-sizer-spectrometer-3321/

50 Prentice, D., Pantoya, M. L., & Gash, A. E. (2006). Combustion wave speeds of sol-gel-synthesized tungsten trioxide and nano-aluminum: The effect of impurities on flame propagation. *Energy & Fuels, 20*(6), 2370-2376.

51 Severac, F., Alphonse, P., Esteve, A., Bancaud, A., & Rossi, C. (2012). High-Energy Al/CuO Nanocomposites Obtained by DNA-Directed Assembly. *Advanced Functional Materials, 22*(2), 323-329.

52 Schoenitz, M., Ward, T. S., & Dreizin, E. L. (2005). Fully dense nano-composite energetic powders prepared by arrested reactive milling. *Proceedings Of the Combustion Institute, 30,* 2071-2078.

53 Zangmeister, C. D., Radney, J. G., Dockery, L. T., Young, J. T., Ma, X., You, R., & Zachariah, M. R. (2014). Packing density of rigid aggregates is independent of scale. *Proceedings of the National Academy of Sciences,111*(25), 9037-9041.

54 NIST Chemistry WebBook. (n.d.). Retrieved April 24, 2015, from http://webbook.nist.gov/chemistry/

55 Smallwood, I. (2012). *Handbook of organic solvent properties*. Butterworth-Heinemann.